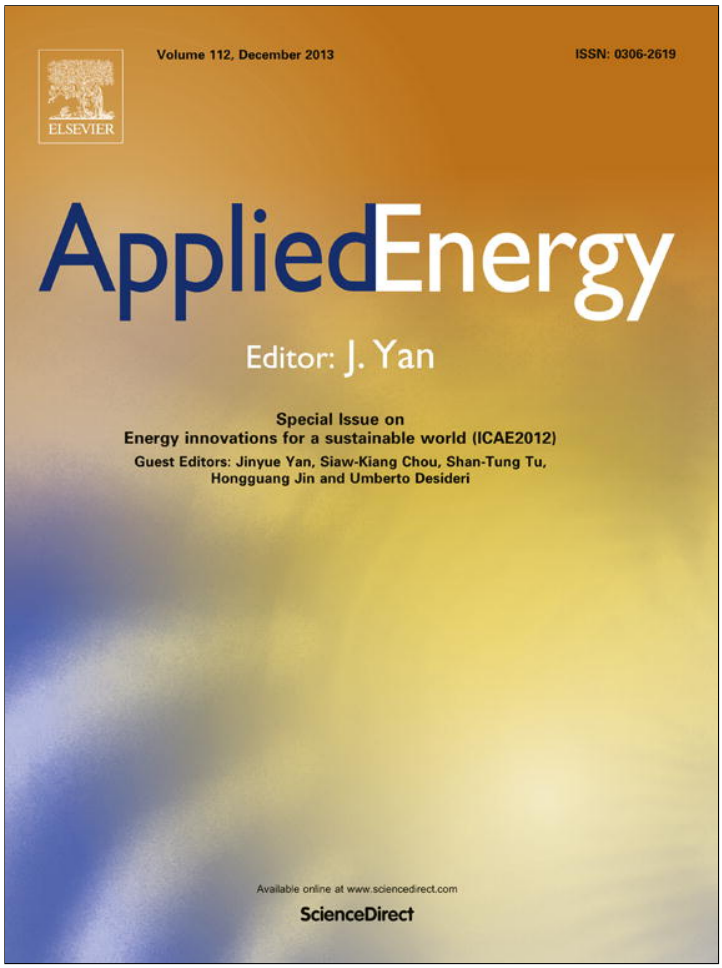

Applied Energy 112 (2013) 1283–1290

Contents lists available at SciVerse ScienceDirect

Applied Energy

journal homepage: www.elsevier.com/locate/apenergy

Stratified two-phase flow pattern modulation in a horizontal tube by the mesh pore cylinder surface

Hongxia Chen [a], Jinliang Xu [a,b,*], Zijin Li [b], Feng Xing [a,b], Jian Xie [a,b]

[a] The Beijing Key Laboratory of New and Renewable Energy, North China Electric Power University, Beijing 102206, PR China
[b] The Beijing Key Laboratory of Multiphase Flow and Heat Transfer, North China, Electric Power University, Beijing 102206, PR China

HIGHLIGHTS

- A phase separation concept was proposed to modulate flow pattern in a tube.
- The cross section of the tube is divided into an annular region and an inner region.
- Stratified flow pattern was successfully modulated.
- Liquid can be within the mesh pore cylinder with gas contacting with the tube wall surface.
- The idea was expected to enhance the condensation heat transfer.

ARTICLE INFO

Article history:
Received 19 September 2012
Received in revised form 26 November 2012
Accepted 26 November 2012
Available online 20 December 2012

Keywords:
Phase separation concept
Condensation
Mesh cylinder
Phase distribution

ABSTRACT

Condensation heat transfer has been studied in the past century due to its wide applications in energy and power systems. The key scientific issue is the thick liquid thickness near the tube wall along the condenser tube length. The fabricated microstructures on the inner wall are the conventional technique to improve the performance. Here a passive phase separation concept was proposed to create distinct phase distribution. An empty cylinder made of a single layer of mesh pore surface was suspended in a tube, dividing the tube into an annular region and an inner region. The mesh pore surface prevents gas phase entering the inner region but sucks liquid towards the inner region. Thus largest possibility for gas directly contacted with the inner wall surface is ensured. An air/water two-phase flow experiment was performed and the stratified flow pattern modulation was investigated. When the liquid level in the horizontal tube is relatively higher, the liquid can be thoroughly within the mesh cylinder to form the "gas-floating-liquid" mode. The whole inner tube wall surface is covered by the gas phase. If the liquid content is relatively smaller, partial liquid can be sucked into the mesh cylinder. The contact area between the inner tube wall and gas is increased. The stratified flow pattern modulation is expected to significantly enhance the condensation heat transfer under low mass fluxes which is being verified by our continuous experiment.

1. Introduction

Condensation is not only a nature phenomenon but also takes place in various industry facilities. A condenser is necessary to dissipate heat to the environment for a thermal power plant and a refrigeration system. An efficient ORC system is a solution to convert low grade thermal energy ($T < 300$ °C) into electricity [1]. The temperature difference between the organic fluid and the environment coolant (air or water) for the condenser is small, yielding a large heat transfer area needed for the condenser. Besides, dynamic variations of the coolant flow rate and temperature make the condenser performance significant deviating from the design condition. The condenser must ensure full condensation of fine bubbles of the organic fluid. Otherwise, the fine gas bubbles attack the rotating blades of the pump to yield the gas-corruption phenomenon, shortening the pump lifetime.

Zhang et al. [2] experimentally investigated the heat transfer characteristics of steam condensation on horizontal twisted elliptical tubes (TETs) with different structural parameters. The steam saturation temperature was about 100.5 °C with the wall subcooling from 2 °C to 14 °C. It is indicated that the condensation heat transfer coefficients for all the tubes reduce with the increase of wall subcooling, while the enhancement factor of each TET is almost constant.

* Corresponding author at: The Beijing Key Laboratory of New and Renewable Energy, North China Electric Power University, Beijing 102206, PR China. Tel./fax: +86 10 61772268.
E-mail address: xjl@ncepu.edu.cn (J. Xu).

0306-2619/$ - see front matter © 2012 Elsevier Ltd. All rights reserved.
http://dx.doi.org/10.1016/j.apenergy.2012.11.062

Nomenclature

Abbreviation

ORC	organic rankine cycle
PPI	pores per inch

Symbols

A	tube cross section area, m^2
D	tube diameter, m
D_σ	the distance between two mesh wires, m
d	mesh pore diameter, m
F	force, N
g	acceleration of gravity, m/s^2
i	array index shown in Fig. 5b
j	array index in the gravity direction (see Fig. 5b)
J	superficial velocity, m/s
$\tilde{J}$	the maximum array number in the vertical direction (see Fig. 5b)
k	array index along the circumference direction (see Fig. 5c)
K	porous permeability, m^2
$\tilde{K}$	the maximum array number along the circumference direction (see Fig. 5c)
p	pressure, Pa
Q	volume flow rates, m^3/s
$Q_{heat,b}$	heat transfer rate in the bare tube along a unit flow length, W/m
$Q_{heat,m}$	heat transfer rate by the modulated flow pattern along a unit flow length, W/m
R	radius of the mesh pore cylinder, m
S_g	circumference length exposed in gas phase, m
T	temperature, °C
u	fluid velocity, m/s
x	coordinate along the flow direction, m

Greek symbols

μ	viscosity, pa·s
ρ	density, kg/m^3
w	mesh pore width, m
σ	surface tension force, N/m
α	wetting angle, °
α_h	heat transfer coefficient, W/m^2K
β	the angle of the line connecting the tube center point and the center of two mesh wires relative to gravity, °
θ	arc angle for the settled liquid over the tube cross section (see Fig. 5c).
ε	porosity of a single layer of mesh
η	heat transfer enhancement ratio
Δ	liquid film thickness surrounding the side mesh pore surface in flow direction, m
ΔT	temperature difference between the tube wall and saturation temperature, K
Δx	the distance for the liquid flow path, m
Δp_c	capillary pressure created by mesh pores, Pa
Δp_l	pressure drop for the liquid flow through the single layer of mesh, Pa

Subscripts

g	gas phase
l	liquid phase
p	mesh pore
eff	effective parameter

Gong et al. [3] performed a thermodynamic analysis for a single stage centrifugal chiller, with the chiller capacity of 1750 kW. The chiller works with the working fluid of R22. The chiller is a combined system due to a heat exchanger arranged between the compressor outlet and the condenser to supply hot water. The phase change (condensation and evaporation) parameters significantly influence the chiller performance. Al-Nimr and AlKam [4] obtained a closed form expression for the film condensation heat transfer on a vertical plate imbedded in a porous media.

Condensation heat transfer is not fully understood even though extensive studies have been performed. Dobson and Chato [5] studied the condensation in smooth horizontal tubes and noted that the heat transfer behavior significantly depended on the flow pattern. At low mass fluxes the smooth/wavy stratified flow pattern occurs, in which liquid phase accumulates on the tube bottom but gas phase is flowing in the upper part of the tube. The tube bottom immersed by liquid has less contribution to the heat transfer. Vapor shear dominated and annular or annular-mist flow prevailed over nearly the entire vapor quality range with forced-convective condensation as the prevailing heat transfer mode at the highest mass fluxes. The heat transfer coefficients are decreased substantially with decreases in vapor qualities and mass fluxes. They are sensitive to the liquid thickness with the condensation development along the flow direction. Lips and Meyer [6] performed the convective condensation of R134a in an 8.38 mm inclined smooth tube. Flow patterns and heat transfer coefficients were presented for different mass fluxes and vapor qualities over the whole range of inclination angles from vertical downwards to upwards. The strong relationship between the heat transfer coefficient and the phase distribution was identified.

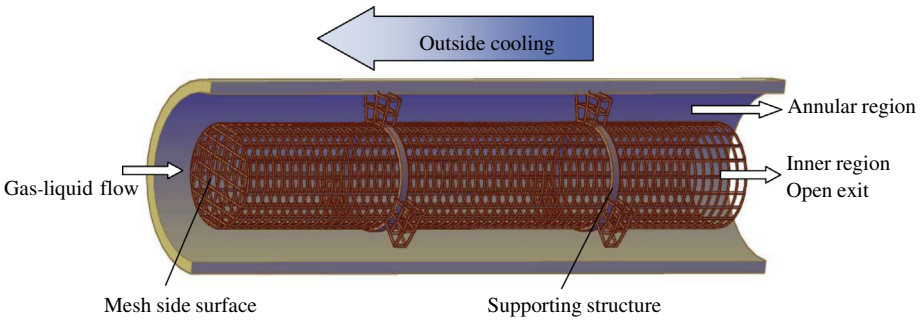

Fig. 1. The newly proposed condenser tube.

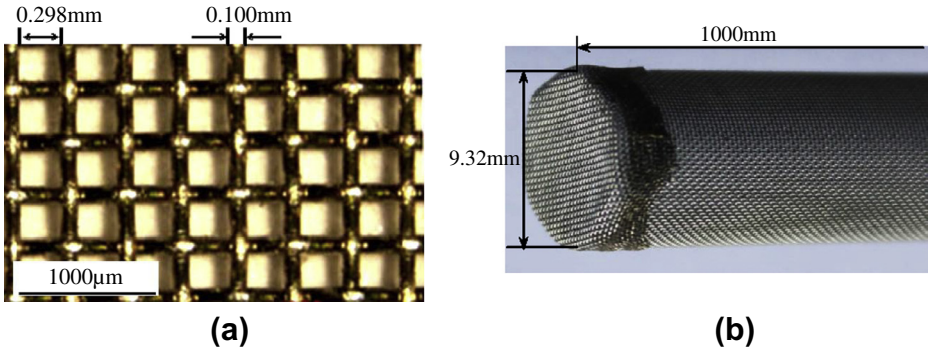

Fig. 2. Stainless steel mesh to fabricate the mesh cylinder (a for the mesh image measured by a microscope, b for the fabricated mesh cylinder).

Generally, liquid tends to populate near the wall and gas tends to accumulate in the tube core. Examination of void fractions over the tube cross-section can deduce such conclusion. For vertical flows the void fraction reaches the maximum at the tube centerline and decrease away from the tube centerline. The horizontal flows have similar phase distribution as the vertical flows. But the void fractions may not be exactly symmetry against the tube centerline. For condensation in tubes, the large liquid thickness near the tube wall separates the tube wall from the saturated vapor to result in a large thermal resistance. In summary, the phase distribution over the tube cross section is not consistent with the condensation heat transfer. Many references reviewed the techniques to improve the condensation heat transfer such as Cavallini et al. [7], Dalkilic and Wongwises [8], Lips and Meyer [9]. These techniques limit the growth of fluid boundary layers locally close to the wall surface.

A passive phase separation concept was proposed to create a distinct phase distribution in the tube cross section to yield good condenser performance in this study. An empty cylinder formed by a single layer of mesh pore surface was suspended in a tube. Thus the gas and liquid phases mainly populated near the tube wall region and the tube core region, respectively. An adiabatic air/water two-phase flow experiment was performed to verify the phase distribution in tubes. The stratified flow pattern modulation results were analyzed and discussed.

2. The condenser tube design and working principle

Fig. 1 shows the condenser tube. Annular flow occurs at the tube upstream when saturated vapor enters the tube. Thus the mesh pore cylinder starts from a specific distance away from the tube inlet. The tube cross section consists of an annular region and an inner region, interfaced by the single layer mesh pore surface. The side cylinder surface has a taper or just a flat shape. The mesh cylinder exit is open. Supporting structure is necessary to ensure the uniform arrangement of the mesh cylinder in the tube.

The mesh pores have two functions: (1) prevent gas bubble entering the inner region; (2) suck liquid towards the inner region. Thus the gas and liquid phases are separated to flow in the two different regions. The mesh pore should have small size to prevent gas bubbles entering the inner region and pump liquid towards the inner region. An effective pore diameter is suggested as $d_{eff} < (\sigma g(\rho_l - \rho_g))^{0.5}$ by Xu and Zhang [10], where σ is the surface tension force, g is the acceleration of gravity, and ρ_l and ρ_g are the liquid and gas densities, respectively. For most gas–liquid systems, d_{eff} is on the order of millimeter.

Fig. 2 shows the stainless steel mesh to fabricate the mesh cylinder. The PPI is 60. The square mesh pores have the characteristic size of 0.3 mm. The stainless steel ligament is 0.1 mm in diameter. The mesh cylinder has an outer diameter of 9.32 mm.

A gas bubble is difficult to enter the mesh cylinder because the surface energy of the gas bubble is increased when it is forced to move from a large space into a small space (see Fig. 3a). The simple surface energy analysis deduces the pressure difference when a large bubble with its size identical to the tube diameter D enters the mesh pore with the width of w as

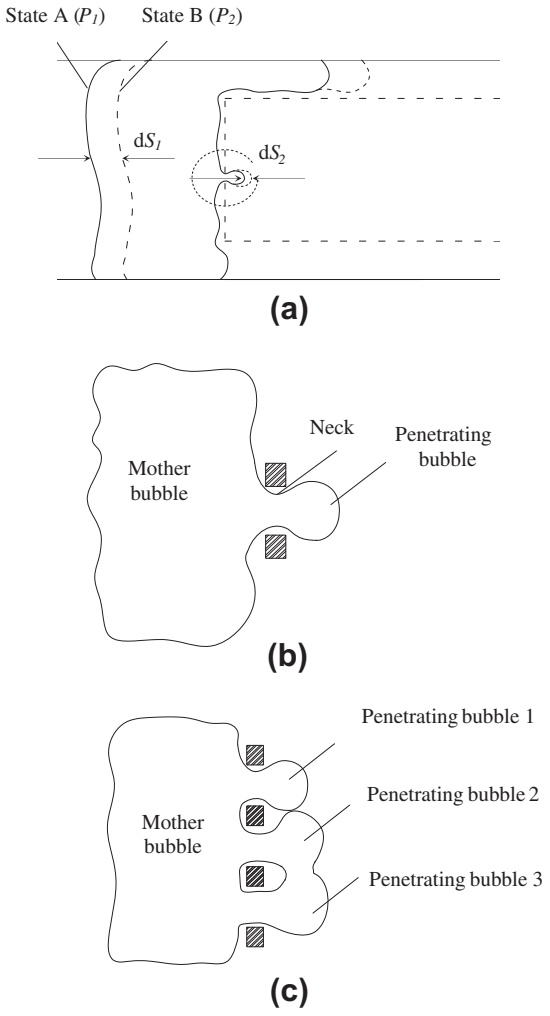

Fig. 3. The mechanism of the mesh pores preventing bubbles entering the mesh cylinder (*a* for pressure difference analysis for a bubble front penetrating over the mesh pore, *b* for the mechanism for the breakup of the bubble neck, and *c* for the coalescence mechanism of many bubble fronts to form large bubble).

$$p_1 - p_2 = 4\sigma\left(\frac{1}{w} - \frac{1}{D}\right) \tag{1}$$

The above equation Eq. (1) shows that because $D>>w$, the second term of the right side of Eq. (1) contributes much less to the pressure difference. Giving $\sigma = 0.07275$ N/m for air/water system at 20 °C and $w = 0.3$ mm, $p_1-p_2 = 970$ Pa, indicating that the pressure difference of more than 970 Pa is necessary to penetrate the front bubble interface in the mesh pore. Penetrating a bubble front over the mesh pore does not mean that such a bubble can successfully enter the mesh cylinder. There are two possible mechanisms for the penetrating bubble to separate from its mother bubble: (1) the viscous force from surrounding liquid (see Fig. 3b), (2) the coalescence of many bubble fronts from the mesh pore array to form a larger bubble (see Fig. 3c).

The driving source for the liquid suction towards the mesh cylinder comes from the capillary pressure (ΔP_c) created by the wick structure, which is expressed as Larson and Morrow [11]

$$\Delta p_c = \frac{4\sigma}{d_{eff}}\cos\alpha \tag{2}$$

where α is the wetting angle. Based on the Darcy's equation, the pressure drop for the liquid flow through the single layer of mesh is

$$\Delta p_l = \frac{\mu_l u_{l,s}}{K}\Delta x \tag{3}$$

where $u_{l,s}$ is the liquid suction velocity through the mesh pores, Δx is the distance for the liquid flow path, K is the porous permeability, expressed as

$$K = \frac{\varepsilon d_p^2}{32} \tag{4}$$

where ε is the porosity of a single layer mesh, d_p is the pore diameter. $\Delta p_c = \Delta p_l$ yields the following expression for the liquid suction velocity:

$$u_{l,s} = \frac{\varepsilon d_p^2 \sigma\cos\alpha}{8\mu_l d_{eff}\Delta x} \tag{5}$$

The maximum liquid suction velocity is estimated as 0.24 m/s assuming $\alpha = 0°$ and $\Delta x = 4.66$ mm (radius of the mesh cylinder).

In order to explain the liquid capturing mechanism within the horizontal tube, we performed the high speed flow visualization of a liquid droplet spreading on a wet mesh pore surface. A piece of mesh pore surface was prepared by the following procedures: (1) rinsed by deionized water; (2) rinsed by acetone in a glass beaker which was put on an ultrasonic platform; (3) dried in an oven; (4) wetted by deionized water in a glass beaker. Then the mesh pore surface was put under a microscope, combined with a high speed camera. An injecting syringe ejects a droplet with its exact volume of 5 μl on the mesh pore surface. The whole dynamic spreading process of the droplet on the wetted mesh pore surface was captured by the high speed camera with a time resolution of 1 ms.

Fig. 4 shows the droplet spreading process. Initially a 5.00 mm diameter water droplet was on the mesh pore surface. With the time elapsed 0.4 s, the liquid droplet diameter was increased to 9.74 mm. Then the droplet was thoroughly within the mesh pores. The water droplet spreading process is caused by the capillary force created by the gas–liquid interface with mesh pores, explaining the mechanism when a stratified flow is approaching the side mesh pore surface, liquid can be sucked over the vertical direction (see A–A cross section in Fig. 5).

Fig. 5 shows the phase distribution of the stratified flow in both the bare tube and flow pattern modulation sections. We focused on the cross section A–A (see Fig. 5b). Each mesh pore with the gas–liquid interface involved is numbered as (i,j) with j as the gravity direction and i perpendicular to the gravity direction. The capillary forced created by the mesh pore $(i,1)$ is

$$F_{\sigma i} = \pi\sigma w\sin\alpha \tag{6}$$

where w is the mesh pore width and α is the contact angle between the gas–liquid interface and the mesh wire. The capillary force given in Eq. (6) is balanced by the total gravity force over the mesh pores (i, j) with j starting from *1* to $\tilde{j}$:

$$F_{\sigma i} = \sum_{j=1}^{\tilde{j}} m_{ij} g \tag{7}$$

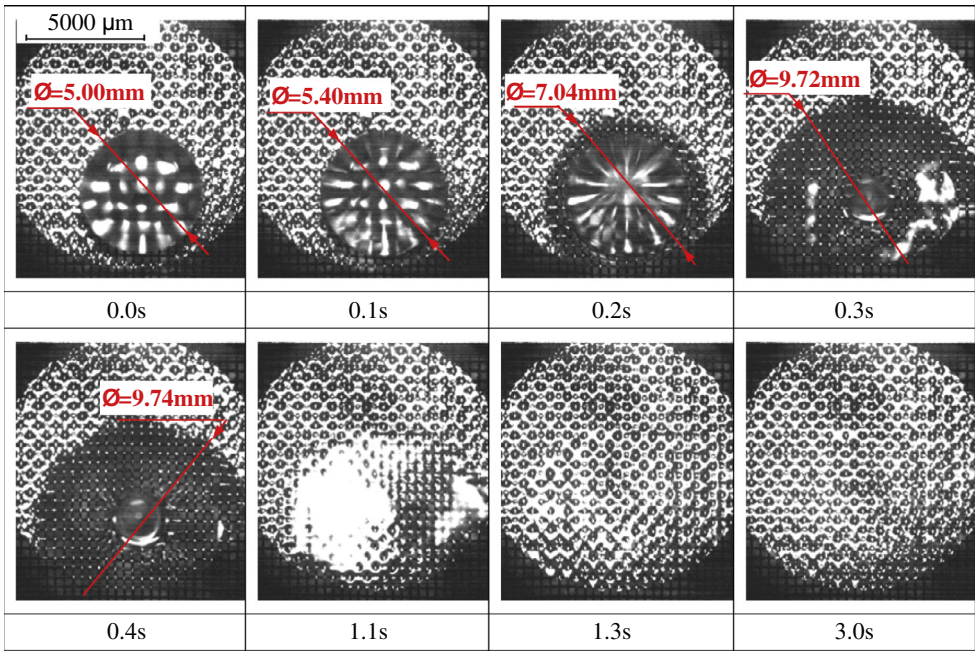

Fig. 4. The spreading process of a droplet on the mesh pore surface.

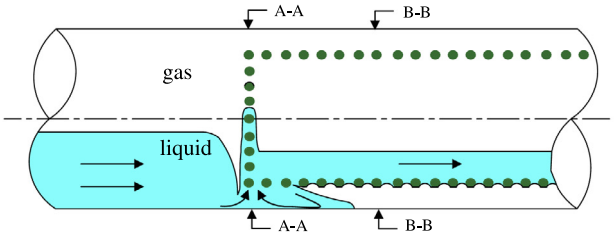

(a) Phase distribution of the stratified flow in bare tube region and flow pattern modulation region

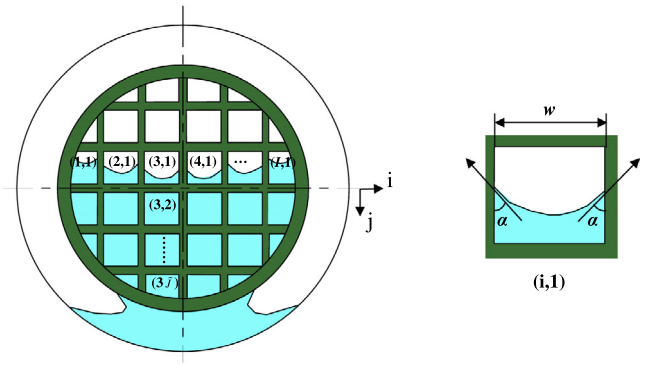

(b) Phase distribution and force analysis over the A-A cross section

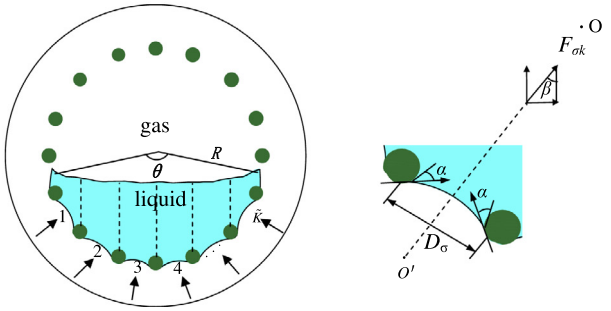

(c) Phase distribution and force analysis over the B-B cross section

Fig. 5. The liquid capture process of stratified flow pattern and force analysis.

where $\tilde{J}$ is the total number of mesh mores for the array j. Eq. (7) is further written as

$$\pi\sigma w \sin\alpha = \rho_l g w^2 \tilde{J} \Delta \tag{8}$$

Thus we obtain the liquid thickness Δ surrounding the mesh pores along the flow direction as

$$\Delta = \frac{\pi\sigma \sin\alpha}{\rho_l g w \tilde{J}} \tag{9}$$

Fig. 5c shows the phase distribution and force analysis over the B-B cross section. Along the circumference direction, the array is marked as k starting from 1 to $\tilde{K}$. Here $\tilde{K}$ is the maximum k array. The total arc angle for the settled liquid over the tube cross section is θ. For the array k, the angle of the line connecting the tube center point and the center of two mesh wires relative to gravity is β see Fig. 5c), which is

$$\beta = \frac{\theta}{2\tilde{K}} + \left(\frac{\theta}{2} - \frac{k\theta}{\tilde{K}}\right) \tag{10}$$

The distance between two mesh wires is D_σ:

$$D_\sigma = 2R \sin\left(\frac{\theta}{2\tilde{K}}\right) \tag{11}$$

The capillary force for the array j shaded in the vertical (gravity) direction is

$$F_{\sigma k} = 2\pi R\sigma \sin\alpha \sin\left(\frac{\theta}{2\tilde{K}}\right) \cos\left(\frac{\theta}{2\tilde{K}} + \left[\frac{\theta}{2} - \frac{k\theta}{\tilde{K}}\right]\right) \tag{12}$$

where R is the mesh cylinder radius. The capillary force given in Eq. (12) for the circumference array j is balanced by the gravity force over the unit marked by the dashed lines (see Fig. 5c).

3. Test section and experimental setup

Two test sections were fabricated: one without and the other with the inserted mesh cylinder (see Fig. 6). Both test sections had a mixer at the entrance with a short tube-in-tube geometry. Inlets 1 and 2 are those for water and air, respectively. Air is discharged into the tube as air jets through capillary holes of needles. The mixer end is defined as the start point of the one-dimensional coordinate x. The two test sections are made of glass so that the flow pattern visualization can be performed.

The glass tube had a length of 2500 mm (not including the mixer), with an inner diameter of 13.08 mm and a tube wall thickness of 2.0 mm. The mesh cylinder starts from x = 1500 mm, with an open end. The annular gap between the tube and the mesh cylinder is 1.88 mm. Two water tanks collect the liquid flow rates from the inner region (outlet 1) and the annular region (outlet 2), respectively (see Fig. 6).

The experiment setup was shown in Fig. 7. A water pump supplies water flow rate to the test section. The water flow rate was measured by one of the two turbine flowmeters, having the ranges of 0.2–2 m^3/h and 0.6–6 m^3/h respectively. Air flow rate was supplied by an air compressor and measured by one of the three rotameters, with the ranges of 16–160 l/h, 0.1–1 m^3/h and 1–10 m^3/h respectively. The water and air flow rates enter the mixer of the test section. All the five flowmeters have accuracies of 0.5% within their own flow rate range. The flow pattern images were captured by a high speed camera. The test section was exactly horizontally positioned. For the test section without the mesh

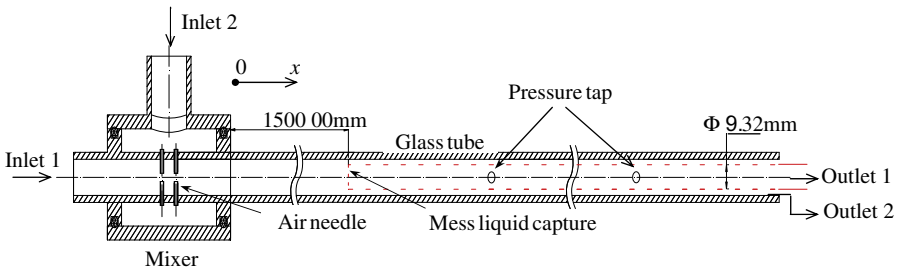

Fig. 6. Test sections for flow pattern measurement (inlet1: water inlet; inlet 2: air inlet; outlet 1: outlet fluid from the mesh cylinder to tank 1; outlet 2: outlet fluid from the annular region to tank 2).

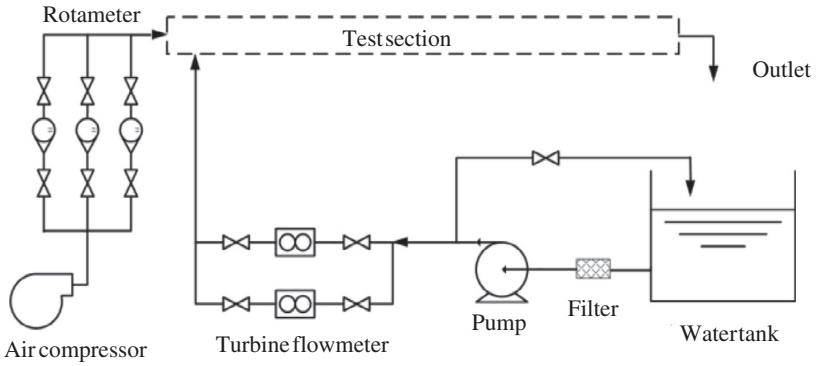

Fig. 7. Experimental setup.

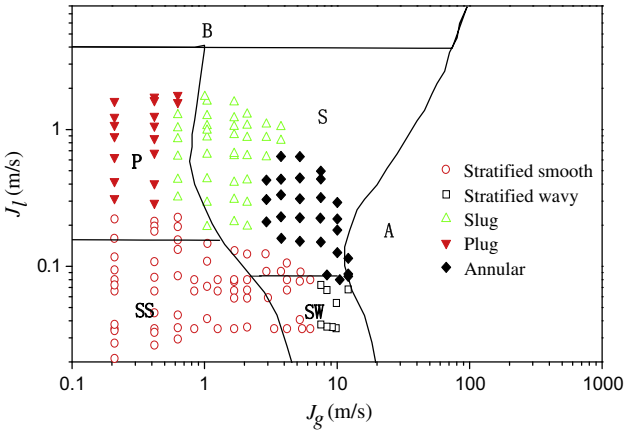

Fig. 8. The flow pattern map in the bare horizontal glass tube and comparison with Mandhane et al. [12] (B: Bubbly flow region; P: Plug flow region; S: Slug flow region; A: Annular flow region; SS: Stratified smooth flow region; SW: Stratified wavy flow region).

cylinder inserted, the fluid at the test section outlet was collected by a tank. The outlet air was discharged into the environment directly but the water was collected by the tank. For the test section with inserted mesh cylinder, two tanks collect the water flow rates from both the inner region and annular region respectively (not shown in Fig. 7).

The superficial velocities of liquid and gas phases are defined as

$$J_l = \frac{Q_l}{A}, \quad J_g = \frac{Q_g}{A} \tag{13}$$

where Q_l and Q_g are the volume flow rates of liquid and gas phases, A is the tube cross section area. During this experiment, J_l and J_g had the ranges of 0.01–2.0 m/s and 0.1–10 m/s respectively.

4. Results and discussion

4.1. Flow patterns in the horizontal glass tube

In order to perform comparisons of flow patterns in horizontal tubes with and without inserted mesh cylinder, flow patterns are examined first in the bare tube. Fig. 8 shows the measured flow pattern map in the 13.08 mm diameter tube. The present measured flow patterns generally match the transition boundaries reported by Mandhane et al. [12]. Flow patterns include the stratified smooth flow, stratified wavy flow, plug flow, slug flow

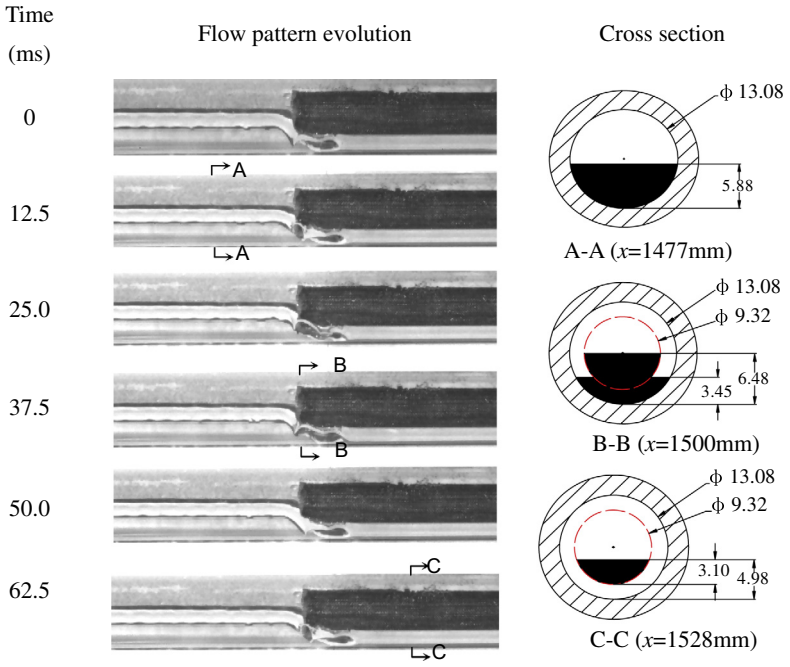

Fig. 9. Flow pattern evolution in different cross sections (full liquid capture case, J_g = 0.335 m/s, J_l = 0.054 m/s, x_s = 1455 mm, x_e = 1555 mm).

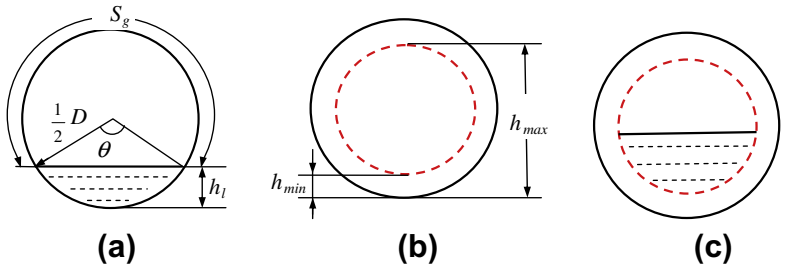

Fig. 10. The geometry configuration for the computation of heat transfer enhancement ratio (*a* for the cross section of bare tube; *b* for the minimum and maximum liquid heights with mesh cylinder inserted; *c* for the liquid within the mesh cylinder).

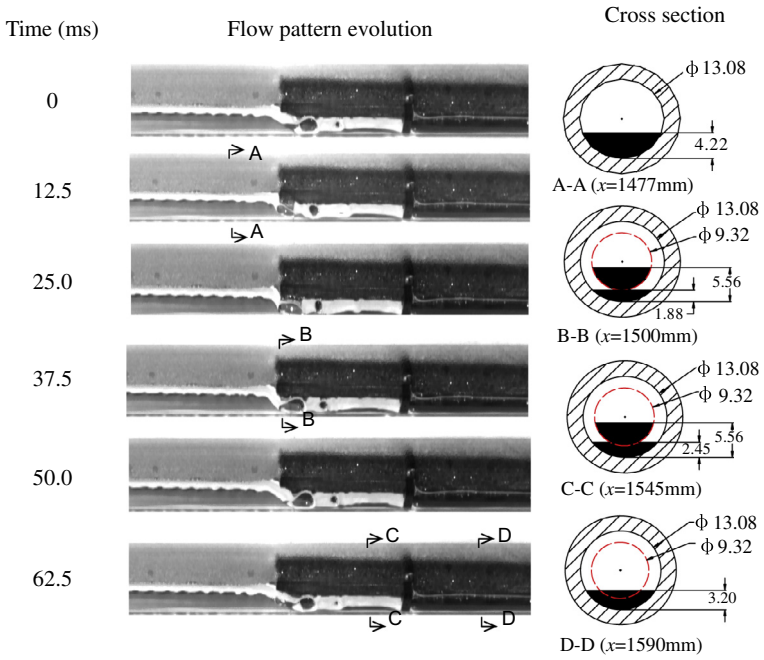

Fig. 11. Flow pattern evolution in different cross sections (partial liquid capture case, J_g = 0.335 m/s, J_l = 0.035 m/s, x_s = 1435 mm, x_e = 1615 mm).

and annular flow. Their descriptions can be found in various two-phase flow and heat transfer textbooks and are not repeated here.

4.2. Stratified flow pattern modulation by the mesh pore cylinder surface

There are two modes for stratified flow pattern modulations by the mesh cylinder: the full liquid capture mode and the partial liquid capture mode.

4.2.1. The full liquid capture case

Fig. 9 shows the transient stratified flow pattern modulation for the first mode. The liquid height from the tube bottom was carefully examined along the flow direction. The liquid and gas phase distribution was illustrated for three cross sections. An initial liquid height of 5.88 mm was maintained at the A–A cross section located at the mesh cylinder upstream. The capillary pumping effect causes different liquid levels in the inner region and the annular region at the B–B cross section. For example, the liquid height was 6.48 mm in the inner region but it was only 3.45 mm in the annular region. The liquid suction process is completed within an axial distance of 13 mm. The C–C cross section demonstrates the state under which all the liquid is within the mesh cylinder, floated by the gas phase in the annular region, called the "gas-floating-liquid" mode. In the vertical direction the capillary force created by mesh pores is balanced by the gravity force of liquid. The contact area between the inner tube wall and gas is 433.3 cm^2/m in the downstream C–C cross section, which is almost two times of 218.4 cm^2/m in the upstream A–A cross section. Because the entire tube cross section is covered by the gas phase, the full liquid capture mode is a wonderful flow pattern modulation for the condensation heat transfer in horizontal tubes at low mass fluxes.

This study is an adiabatic two-phase measurement of the flow pattern modulation. It is important to estimate the degree that the enhanced condensation heat transfer can be reached for a practical ORC application. This is because the heat transfer area is large due to the pool heat transfer characteristic by using the organic fluid. Fig. 10a shows the geometry configuration in the bare tube section. The heat transfer rate is directly related to the tube surface area exposed in the vapor phase:

$$Q_{heat,b} = \alpha_h \cdot \Delta T \cdot S_g \tag{14}$$

where $Q_{heat,b}$ is the heat transfer rate in the bare tube along a unit flow length, α_h is the thin film condensation heat transfer coefficient, ΔT is the temperature difference between the tube wall and the saturation temperature and S_g is the circumference length exposed in the vapor phase. When the liquid height is h_l (see Fig. 10a), S_g is

$$S_g = \pi D - D \cdot \arccos\left(1 - \frac{2h_l}{D}\right) \tag{15}$$

Fig. 10b shows the range of liquid height h_l in the bare tube to be modulated by the mesh cylinder, in which h_{min} and h_{max} are the liquid levels that contact with the mesh cylinder bottom and mesh cylinder top, respectively. The flow pattern modulation makes all the liquid within the mesh cylinder (see Fig. 10c). The heat transfer rate along a unit flow length becomes

$$Q_{heat,m} = \alpha_h \cdot \Delta T \cdot S \tag{16}$$

where S is the tube circumference ($S = \pi D$). By comparing Eqs. (14) and (16), the enhanced condensation heat transfer factor is defined as

$$\eta = \frac{Q_{heat,m}}{Q_{heat,b}} = \frac{S}{S_g} = \frac{1}{1 - \arccos(1 - \frac{2h_l}{D})/\pi} \tag{17}$$

Substituting h_{min} = 1.88 mm and h_{max} = 11.20 mm into Eq. (17), the heat transfer enhancement ratio reaches $1.33 \leqslant \eta \leqslant 4.04$. In other words, the heat transfer by the modulated flow can be four times of that in the bare tube under the stratified flow pattern.

4.2.2. The partial liquid capture case

The liquid height is decreased with decreases in the liquid superficial velocities. At relatively lower liquid height, part of liquid can be captured by the mesh cylinder. Seeing from Fig. 11, the bare tube section holds an initial liquid height of 4.22 mm. The B–B cross section in Fig. 11 shows a higher liquid height of 5.56 mm in the mesh cylinder but a lower liquid height of 1.88 mm in the annular region. Further flow evolution yields the liquid heights of 5.56 mm in the mesh cylinder and 2.45 mm in the annular region (see the C–C cross section in Fig. 11). The steady state shown in the D–D cross section holds the same liquid heights of 3.20 mm in both the inner region and annular region. The lower liquid height of 3.20 mm in the D–D cross section than the initial liquid height of 4.22 mm in the bare tube is caused by the liquid speeding up due to the capillary force by mesh pores along the flow direction. By comparing Figs. 9 and 11, the initial liquid wetting perimeter along the mesh cylinder circumference plays an important role on the liquid hold up in the gravity direction (vertical direction). A very low liquid superficial velocity may not cause the full "gas-floating-liquid" mode, but the contacted area between the tube inner wall surface and the gas phase is increased.

5. Conclusions

Suspending an empty mesh cylinder in a horizontal tube could modulate flow patterns. Due to miniature pore size used, gas bubble is difficult to enter the mesh cylinder but liquid can be sucked towards the mesh cylinder. An air–water two-phase flow experiment was performed to verify the idea. If there is a relatively higher liquid level in the bare horizontal tube, all the liquid can be captured by the mesh cylinder to form the "gas-floating-liquid" mode. For a lower liquid height in the horizontal tube, partial liquid can be sucked by the mesh cylinder, and the contact area between the tube wall and the gas is increased. For both the full and partial liquid capture cases, the condensation heat transfer should be enhanced due to the gas phase populated near the tube wall, thus the perfect thin liquid film condensation heat transfer mechanism can be ensured.

Acknowledgements

This work was supported by the Natural Science Foundation of China with the contract number of 51106050, the National Basic Research Program of China with the contract number of 2011CB710703, the Natural Science Foundation of China of International cooperation project with the contract number of 51210 011, and the Beijing Science and Technology Program (Z1111 09055311097).

References

[1] David JS, Neil L. Organic rankine cycle working fluid considerations for waste heat to power applications. ASHRAE Trans 2010;116(1):525–33.
[2] Zhang L, Yang S, Xu H. Experimental study on condensation heat transfer characteristics of steam on horizontal twisted elliptical tubes. Appl Energy 2012;97:881–7.
[3] Gong GC, Chen FH, Su H, Zhou JY. Thermodynamic simulation of condensation heat recovery characteristics of a single stage centrifugal chiller in a hotel. Appl Energy 2012;91:326–33.
[4] Al-Nimr MA, AlKam MK. Film condensation on a vertical plate imbedded in a porous medium. Appl Energy 1997;56(1):47–57.
[5] Dobson MK, Chato JC. Condensation in smooth horizontal tubes. J Heat Transfer 1998;120:193–213.
[6] Lips S, Meyer JP. Experimental study of convective condensation in an inclined smooth tube. Part I: Inclination effect on flow pattern and heat transfer coefficient. Int J Heat Mass Transf 2012;55:395–404.
[7] Cavallini A, Censi G, Del Col D, Doretti L, Longo GA, Rossetto L, et al. Condensation inside and outside smooth and enhanced tubes-a review of recent research. Int J Refrig 2003;26:373–92.
[8] Dalkilic AS, Wongwises S. Intensive literature review of condensation inside smooth and enhanced tubes. Int J Heat Mass Transf 2009;52(15–16):3409–26.
[9] Lips S, Meyer JP. Two-phase flow in inclined tubes with specific reference to condensation: a review. Int J Multiphas Flow 2011;37:845–59.
[10] Xu JL, Zhang XM. Start-up and steady thermal oscillation of a pulsating heat pipe. Heat Mass Transf 2005;41(8):685–94.
[11] Larson RG, Morrow NR. Effects of sample size on capillary pressures in porous media. Powder Technol 1981;30(2):123–38.
[12] Mandhane JM, Gregory GA, Aziz K. A flow-pattern map for gas-liquid flow in horizontal pipe. Int J Multiphas Flow 1974;1(04):537–53.